

## Article

# Copper Supported on MgAlO<sub>x</sub> and ZnAlO<sub>x</sub> Porous Mixed-Oxides for Conversion of Bioethanol via Guerbet Coupling Reaction

Zongyang Liu <sup>1,†</sup>, Jie Li <sup>1,†</sup>, Yuan Tan <sup>1,\*</sup>, Luyao Guo <sup>1</sup> and Yunjie Ding <sup>1,2,3,\*</sup><sup>1</sup> Hangzhou Institute of Advanced Studies, Zhejiang Normal University, Hangzhou 311231, China<sup>2</sup> Dalian National Laboratory for Clean Energy, Dalian Institute of Chemical Physics, Chinese Academy of Sciences, Dalian 116023, China<sup>3</sup> The State Key Laboratory of Catalysis, Dalian Institute of Chemical Physics, Chinese Academy of Sciences, Dalian 116023, China

\* Correspondence: yuantan2012@zjnu.edu.cn (Y.T.); dyj@dicp.ac.cn (Y.D.); Tel.: +86-571-82257902 (Y.T.); +86-411-84379143 (Y.D.)

† These authors contributed equally to this work.

**Abstract:** The direct conversion of biomass-derived ethanol to high-valued-added chemicals has attracted widespread attention recently due to the great economic and environmental advantages. In the present study, the conversion of bioethanol through the Guerbet coupling process was studied in a fixed-bed reactor for MgAlO<sub>x</sub> and ZnAlO<sub>x</sub> mixed-oxides supported Cu catalysts. From the results, Cu adding into the system greatly enhance the dehydrogenation of ethanol and increase the H-transfer in the course of Guerbet coupling process. Simultaneously, the porous mixed-oxides provide the acid-base property of the catalysts for intermediate transformation. Notably, for Cu/MgAlO<sub>x</sub>, the main product of ethanol conversion is butanol, but for Cu/ZnAlO<sub>x</sub>, the primary product is ethyl acetate. Characterizations such as X-ray diffraction (XRD), high-resolution transmission electron microscopy (HRTEM), X-ray photoelectron spectroscopy (XPS), in situ diffuse reflectance infrared Fourier transform spectroscopy (DRIFTS) and CO<sub>2</sub> temperature programmed desorption (TPD) were carried out to evaluate the structure and property of the catalysts. In combination with the catalytic performances with the characterization results, the synergistic catalytic effect between metal sites and acid-base sites were elaborated.

**Keywords:** Cu catalyst; mixed-oxide; bioethanol; Guerbet coupling; butanol

**Citation:** Liu, Z.; Li, J.; Tan, Y.; Guo, L.; Ding, Y. Copper Supported on MgAlO<sub>x</sub> and ZnAlO<sub>x</sub> Porous Mixed-Oxides for Conversion of Bioethanol via Guerbet Coupling Reaction. *Catalysts* **2022**, *12*, 1170. <https://doi.org/10.3390/catal12101170>

Academic Editors: Victorio Cadierno, Raffaella Mancuso and Ioannis D. Kostas

Received: 30 August 2022

Accepted: 27 September 2022

Published: 4 October 2022

**Publisher's Note:** MDPI stays neutral with regard to jurisdictional claims in published maps and institutional affiliations.



**Copyright:** © 2022 by the authors. Licensee MDPI, Basel, Switzerland. This article is an open access article distributed under the terms and conditions of the Creative Commons Attribution (CC BY) license (<https://creativecommons.org/licenses/by/4.0/>).

## 1. Introduction

Over the past decades, due to the increased depletion of fossil feedstock, the demand for alternate and renewable energy is continuously growing [1,2]. Ethanol is a versatile and sustainable raw material which can be produced from the fermentation of renewable biomass such as sugars and corns [3,4]. Currently, bioethanol is widely used as a fuel additive, blending with gasoline for partly replacing traditional fossil fuels [5,6]. However, when compared with gasoline, ethanol has some major drawbacks, such as low energy density (19.6 MJ·L<sup>-1</sup>), high water solubility, and corrosion compared to the current technology of engines and fuel infrastructure [7–10]. Compared to ethanol, butanol has larger energy density (29.2 MJ·L<sup>-1</sup>) and lower miscibility in water. Thus, it is considered as a potential gasoline fuel additive and “advanced biofuel” with good environmental benefits [8,9]. In addition to use as a biofuel, butanol can be also utilized as an important raw bulk material in the manufacture of paints, solvents, and plasticizers [11,12].

Traditionally, *n*-butanol is produced through fossil-based oxo process or the fermentation of sugar-containing crops (ABE process) [13,14]. Alternatively, with the increased

availability of ethanol from biomass, the direct conversion of ethanol into butanol has been proposed to be an economical and sustainable route for butanol production [15–18]. The Guerbet coupling reaction, corresponding to the catalytic conversion of light alcohols into higher ones, have recently attracted widespread attention [19,20]. Several heterogeneous catalysts such as hydroxyapatites (HAP) [21,22], metal oxides [8,12,23], activated carbon [17,24,25], and molecular sieves [26] were utilized to convert ethanol into higher alcohols through the Guerbet coupling process. However, under the present catalytic systems, the reaction condition needs to be performed at high temperatures (generally above 623 K) [12,21,26]. Thus, many researchers have tried their best to decrease the operating temperature and increase the activity of catalysts by adding metal species [14,27–30].

Hydrotalcite (HT) derived mixed oxides supported copper catalysts have been found to be a good candidate for the Guerbet coupling process due to the synergistic effect between metal species and mixed oxides by coupling dehydrogenation/hydrogenation process and condensation reactions for ethanol transformation [23,27,28]. For example, Cu/Mg<sub>x</sub>AlO<sub>y</sub> catalysts with low Cu loadings (0.1–0.6 wt.%) exhibited high selectivity (49–63%) to linear chain C<sub>4</sub>+ alcohols [28]. Cu has been proven to have a promotional effect on the reaction rates of H-transfers, accelerating acid-base-catalyzed deprotonation and hydrogenation/dehydrogenation steps. Cu modified NiMgAlO catalysts were reported to improve ethanol conversion and butanol selectivity at moderate reaction conditions (523 K) [27]. The presence of Cu species was supposed to create Lewis acid-base pairs and CuNi alloy sites, thus increasing H-transfer and condensation reactions, resulting in elevated ethanol conversion (30%) and butanol selectivity (64.2%). Recently, our group found that Cu supported on NiAlO<sub>x</sub> exhibited good performance and stability in the Guerbet coupling process [31]. An optimal compromise between the ethanol conversion (~35%) and butanol selectivity (~45%) has to be sustained for the 0.75%Cu/NiAlO<sub>x</sub> catalyst for 1000 h at 523 K [31]. However, for the above catalysts, the effect of support was seldomly elaborated, which in most cases, influencing the property and performances of the catalysts [32–35]. Additionally, the product distribution of the Guerbet coupling process was highly related with the support effect when synthesized with other valuable chemicals such as acetaldehyde, ethyl acetate, ether, butadiene, etc. [32,35].

This research aims to investigate the MgAlO<sub>x</sub> and ZnAlO<sub>x</sub> porous mixed-oxides supported Cu catalysts for ethanol conversion to butanol via Guerbet coupling reaction. With similar synthesis process and Cu contents, the catalytic performance and stability of both catalysts were studied systematically. N<sub>2</sub>-physical adsorption-desorption, X-ray diffraction (XRD), transmission electron microscopy (TEM), and X-ray photoelectron spectroscopy (XPS) were carried out to evaluate the geometric structure and electronic property of the catalysts. Additionally, CO<sub>2</sub> temperature programmed desorption (TPD), pyridine adsorbed Fourier-transformed infrared absorption spectra (FT-IR), and in situ diffuse reflectance infrared Fourier transform spectroscopy (DRIFTS) were employed to test the acid-base property and adsorptive property of the catalysts, from which the relationship between the property and catalytic performances were accordingly revealed.

## 2. Results and Discussion

### 2.1. Catalytic Performances

The catalytic performance of MgAlO<sub>x</sub> and ZnAlO<sub>x</sub> porous mixed-oxides supported Cu catalysts for ethanol conversion were carried out in a continuous fixed-bed reactor at 553 K and 2 MPa of N<sub>2</sub>. For comparison, pure mixed-oxides without addition of Cu were carried out for this reaction under the identical reaction conditions. From Table 1, MgAlO<sub>x</sub> and ZnAlO<sub>x</sub> (entries 1 and 2) showed very low activity for ethanol, with values of 4.4% and 8.5%, respectively. In addition, the selectivity of butanol was very low for the above mixed-oxides. Nevertheless, when Cu was added into the mixed-oxides, ethanol conversion was greatly enhanced to 43.1% for Cu/MgAlO<sub>x</sub> (Table 1, entry 3) and 33.9% for Cu/ZnAlO<sub>x</sub> (Table 1, entry 4). Simultaneously, the selectivity of butanol for Cu/MgAlO<sub>x</sub>

greatly increased to 33.2%, accomplished by major byproducts of ethyl acetate (Sel. 11.8%), butaldehyde (Sel. 8.6%), ethyl butyrate (Sel. 5.0%), and hexanol (Sel. 8.0%). Such results are comparable or better than the previous results, in which a good compromise between ethanol conversion and butanol selectivity was pursued [23,31,34]. In contrast, the main product on the Cu/ZnAlO<sub>x</sub> was ethyl acetate, with the selectivity of 42.2%, which is widely used in paints, coatings, inks, and adhesives. Other byproducts, such as butanol (Sel. 7.7%), ether (Sel. 1.8%), butaldehyde (Sel. 9.4%) and ethyl butyrate (Sel. 8.3%), can be also detected. Thus, the results suggested Cu species could facilitate the transformation of ethanol in the Guerbet coupling process, both in the Cu/MgAlO<sub>x</sub> and Cu/ZnAlO<sub>x</sub> catalytic systems. However, the support effect also makes a big difference on the distribution of products, implying a synergistic effect between Cu and mixed-oxides on the Guerbet coupling process.

**Table 1.** Catalytic activities of mixed oxides and supported Cu catalysts for ethanol conversion.

Entry	Catalysts	Conversion (%)	Selectivity (%)					
			Butanol	Ethyl Acetate	Ether	Butaldehyde	Ethyl Butyrate	Hexanol
1	MgAlO <sub>x</sub>	4.4	0	0.7	1.5	1.5	0	0
2	ZnAlO <sub>x</sub>	8.5	0.2	38.6	0	2.1	1.5	0
3	Cu/MgAlO <sub>x</sub>	43.1	33.2	11.8	0	8.6	5.0	8.0
4	Cu/ZnAlO <sub>x</sub>	33.9	7.7	42.2	1.8	9.4	8.3	0

Reaction conditions: Catalyst: 1 g, T = 553 K, P<sub>N<sub>2</sub></sub> = 2 MPa, GHSV = 692 h<sup>-1</sup>, LHSV = 4.8 h<sup>-1</sup>.

To further evaluate the products distribution and stability of above catalysts, a time on stream (TOS) of above 100 h was performed for the Cu/MgAlO<sub>x</sub> and Cu/ZnAlO<sub>x</sub> catalysts for the Guerbet coupling process. The results are displayed in Figure 1. From Figure 1a, the major product of Cu/MgAlO<sub>x</sub> is butanol, with selectivity preserving in the range of 30–33%. Other byproducts including ethyl acetate, butane, butaldehyde, hexanol, ethyl butyrate, etc. can be also detected. However, the selectivities were all below 10%. Undetectable gas byproducts or liquid products might also be formed in the process, which account for 20% of the carbon mass loss. In addition, Cu/MgAlO<sub>x</sub> catalyst exhibited an obvious deactivation feature, with ethanol conversion decreased from 43% to 33% after a TOS of 108 h. Unlike the Cu/MgAlO<sub>x</sub>, the main product of the Cu/ZnAlO<sub>x</sub> is ethyl acetate, with the selectivity maintained at 40–42% (Figure 1b). Butane, butanol, ethyl butyrate, etc. appeared as the main byproducts. Except for a slight decrease in initial 24 h, the conversion of ethanol for Cu/ZnAlO<sub>x</sub> is preserved in the range of 29–33%, implying an excellent stability of Cu/ZnAlO<sub>x</sub> catalyst for ethanol conversion.

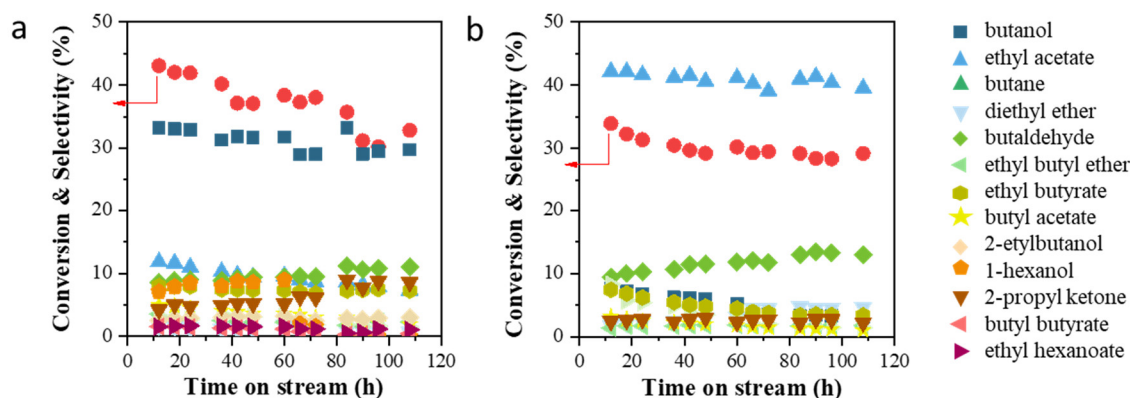


**Figure 1.** The products distributions of reaction with time courses for the (a) Cu/MgAlO<sub>x</sub> and (b) Cu/ZnAlO<sub>x</sub> catalysts. Reaction conditions: amounts of catalyst: 1 g; pressure of N<sub>2</sub>: 2 MPa; temperature: 553K; GHSV: 692 h<sup>-1</sup>, LHSV: 4.8 h<sup>-1</sup>.

## 2.2. Structure of the Catalysts

N<sub>2</sub>-physical adsorption-desorption was evaluated to test the pore structure of catalysts such as the specific surface area ( $S_{\text{BET}}$ ), pore volume, and pore width (as displayed in Table 2). The isotherms and BJH pore size distribution curves are displayed in Figure 2. From the results, MgAlO<sub>x</sub> and ZnAlO<sub>x</sub> showed  $S_{\text{BET}}$  of 119.7 and 155.9 m<sup>2</sup>/g, respectively. However, as Cu species was added, a decrease in  $S_{\text{BET}}$  and pore volume were observed in Cu/MgAlO<sub>x</sub> and Cu/ZnAlO<sub>x</sub> catalysts, which could be attributed to the deposition of Cu species inside the pores of mixed oxides. Furthermore, the isothermal curves of above samples show obvious type IV hysteresis loops according to IUPAC classification, indicating the presence of porous structure in the above samples [36,37]. Additionally, the contents of Cu for the Cu/MgAlO<sub>x</sub> and Cu/ZnAlO<sub>x</sub> catalysts were measured by inductively coupled plasma atomic emission spectroscopy (ICP-AES), with the similar values of 1.11 wt.% and 1.35 wt.%, which also agreed well with the nominal values.

**Table 2.** Textural properties of mixed oxides and supported Cu catalysts.

Entry	Catalyst	Loadings of Cu (%)	Surface Area (m <sup>2</sup> /g)	Pore Volume (cm <sup>3</sup> /g)	Half Pore Width (nm)
1	MgAlO <sub>x</sub>	-	119.7	0.44	12.69
2	ZnAlO <sub>x</sub>	-	155.9	0.30	3.43
3	Cu/MgAlO <sub>x</sub>	1.11	101.5	0.36	4.87
4	Cu/ZnAlO <sub>x</sub>	1.35	115.7	0.25	1.71

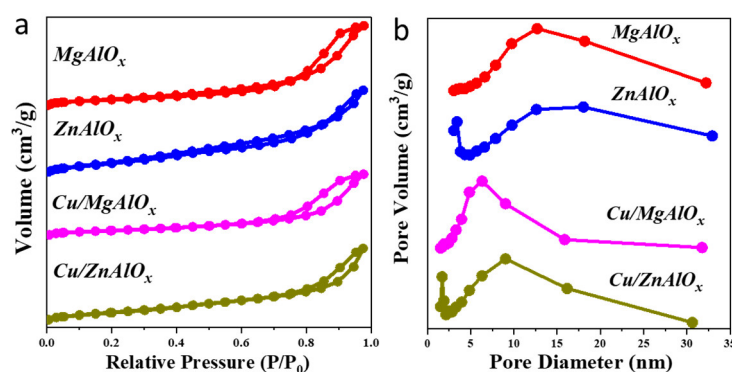


**Figure 2.** (a) N<sub>2</sub> physical adsorption-desorption isotherms and (b) BJH-pore size distributions of mixed oxides and supported Cu catalysts.

The powder XRD patterns of Cu/MgAlO<sub>x</sub> and Cu/ZnAlO<sub>x</sub> catalysts are displayed in Figure 3. From the results, both catalysts show characteristic peaks of corresponding oxides (MgO or ZnO), which derived from the collapse of layered hydrotalcite structure. The absence of Al<sub>2</sub>O<sub>3</sub> phase in the two catalysts indicated an amorphous state of Al<sub>2</sub>O<sub>3</sub> or homogeneous dispersion of Al<sub>2</sub>O<sub>3</sub> inside the mixed oxides. In addition, in the Cu/MgAlO<sub>x</sub> and Cu/ZnAlO<sub>x</sub> catalysts, no diffraction peaks ascribed to Cu nanoparticles could be observed, indicating a uniform dispersed Cu species or low concentration of Cu on the surface.

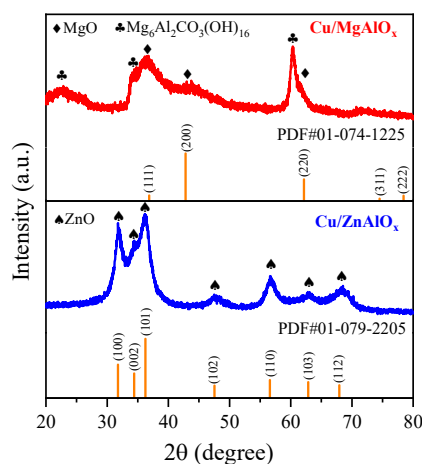


**Figure 3.** XRD patterns of different supported Cu catalysts.

In order to get the structural information and lattice parameters of above catalysts, TEM and HRTEM were performed on the Cu/MgAlO<sub>x</sub> (Figure 4a,c) and Cu/ZnAlO<sub>x</sub> (Figure 4b,d) catalysts. From TEM images (Figure 4a,b), no obvious particles could be observed in the above samples, implying Cu species were highly dispersed on the surface of the catalysts. In addition, the interplanar spacing of  $\sim 2.14$  Å and  $\sim 2.86$  Å corresponding to MgO (200) and ZnO (100) lattice fringes could be discerned for Cu/MgAlO<sub>x</sub> and Cu/ZnAlO<sub>x</sub> (Figure 4d), implying the major phase of above catalysts is corresponding oxides, which was consistent with the XRD results.

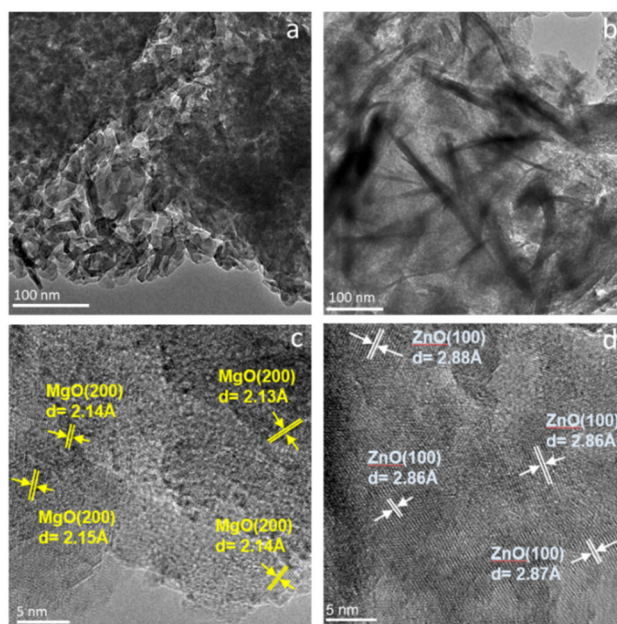


**Figure 4.** TEM and HRTEM images of different supported Cu catalysts: (a,c) Cu/MgAlO<sub>x</sub>; (b,d) Cu/ZnAlO<sub>x</sub>.

### 2.3. Electronic Property of the Catalyst

The surface composition of Cu/MgAlO<sub>x</sub> and Cu/ZnAlO<sub>x</sub> catalysts were measured by X-ray photoelectron spectroscopy (XPS). The C 1s, Cu 2p, O 1s, and Al 2p XPS spectra are shown in Figure 5. The binding energies (B.E.) of the above elements were referenced; the B.E. of C 1s core level at 284.8 eV (Figure 5a) [38]. Figure 5b shows the Cu 2p XPS spectra of Cu/MgAlO<sub>x</sub> and Cu/ZnAlO<sub>x</sub> catalysts. A couple of peaks located at 933.0 eV and 952.8 eV were ascribed to Cu 2p<sub>3/2</sub> and Cu 2p<sub>1/2</sub>, respectively [27,39]. The Cu 2p<sub>3/2</sub> at 933.0 eV and

934.8 eV should be assigned to  $\text{Cu}^+/\text{Cu}^0$  and  $\text{Cu}^{2+}$  species [31,39]. Noteworthy, the Cu species of the  $\text{Cu}/\text{MgAlO}_x$  are almost  $\text{Cu}^+/\text{Cu}^0$ , whereas for the  $\text{Cu}/\text{ZnAlO}_x$ , except for  $\text{Cu}^+/\text{Cu}^0$ ,  $\text{Cu}^{2+}$  species also existed on the surface, as proved by the coexistence of satellite peaks at 940–945 eV [39,40]. Figure 5c shows the O 1s XPS spectra of the two catalysts. From the results, two distinct peaks at 531.6 eV and 530.2 eV were observed and should be ascribed to the existence of adsorbed oxygen ( $\text{O}_\alpha$ ) and lattice oxygen ( $\text{O}_\beta$ ) [27,41]. The relative amounts of  $\text{O}_\alpha$  and  $\text{O}_\beta$  changed with the composition of supports, suggesting that the chemical form of surface oxygen depends heavily on the chemical composition. Obviously, the  $\text{Cu}/\text{MgAlO}_x$  has more  $\text{O}_\alpha$  than that of the  $\text{Cu}/\text{ZnAlO}_x$ , indicating that oxygen molecules prefer to accumulate on the surface of the  $\text{Cu}/\text{MgAlO}_x$  in the form of a hydroxyl group, which might provide some basic sites to the catalysts [27]. In contrast, for the  $\text{Cu}/\text{ZnAlO}_x$  catalyst, more  $\text{O}_\beta$  were present on the surface, suggesting that oxygen appears in the form of metal oxides, i.e.,  $\text{ZnO}$  or  $\text{Al}_2\text{O}_3$ . In addition, in the Al 2p XPS spectra (Figure 5d), the binding energy at 73.8–74.2 eV could be assigned to  $\text{Al}^{3+}$ , which corresponded to the Zn-O-Al and Mg-O-Al, respectively [41].

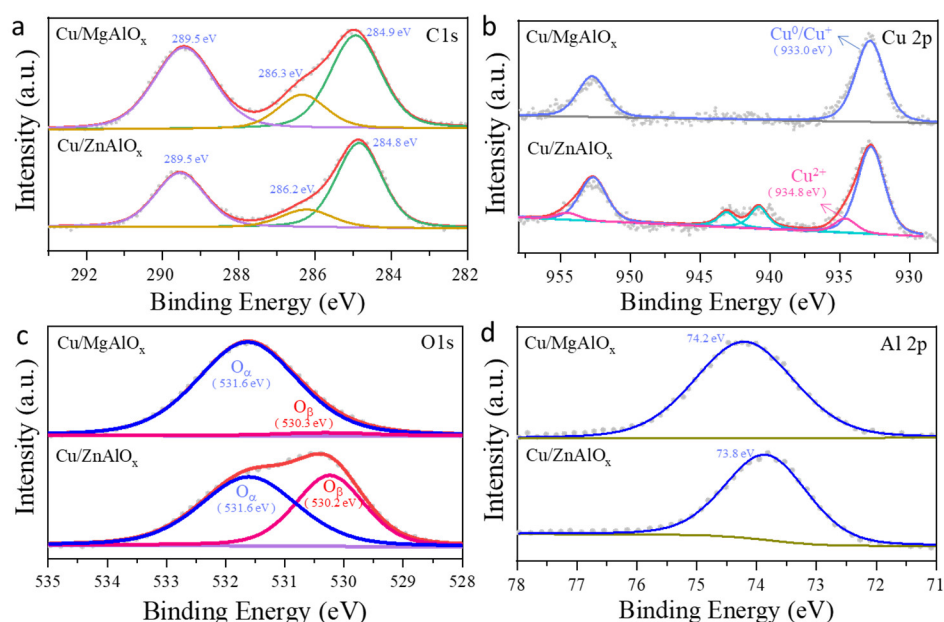


**Figure 5.** XPS spectra of different supported Cu catalysts: (a) C 1s; (b) O 1s; (c) Cu 2p; and (d) Al 2p.

#### 2.4. The Acid-Basic Property of the Catalyst

Figure 6 shows the  $\text{CO}_2$  temperature-programmed desorption (TPD) profiles and pyridine adsorbed FT-IR spectra of the supported Cu catalysts. From the results, the acid-basic property of the  $\text{Cu}/\text{MgAlO}_x$  and  $\text{Cu}/\text{ZnAlO}_x$  catalysts were thereby compared. In Figure 6a, the surface basicity has been determined by  $\text{CO}_2$ -TPD. In the range of 100–900 °C, the  $\text{CO}_2$  desorption peaks can be deconvoluted into four contributions, which could be assigned to the weak (< 250 °C), moderate (250–470 °C), strong (470–650 °C), and super strong basic sites (> 650 °C), respectively [42,43]. For  $\text{Cu}/\text{MgAlO}_x$ , a large amount of moderate basic sites can be observed in  $\text{CO}_2$ -TPD profiles, and the intensity is 10 times higher than that of  $\text{Cu}/\text{ZnAlO}_x$ . Based on O 1s XPS spectra (Figure 5b), the moderate basic sites might derive from the surface hydroxyl group [33,43], whereas for the  $\text{Cu}/\text{ZnAlO}_x$ , more lattice oxygen contributes to the strong and super strong basic sites [33,43]. In order to determine surface acidity, in situ FT-IR of pyridine adsorbed on  $\text{Cu}/\text{MgAlO}_x$  and  $\text{Cu}/\text{ZnAlO}_x$  were measured separately. The distribution of Brønsted and Lewis acid sites were determined in the range of 1300–1700  $\text{cm}^{-1}$ . As seen in Figure 6b, the absence of a band positioned at 1540  $\text{cm}^{-1}$  in  $\text{Cu}/\text{MgAlO}_x$  and  $\text{Cu}/\text{ZnAlO}_x$  reflects the lack of Brønsted acid sites (B), whereas the band at 1450  $\text{cm}^{-1}$  corresponding to pyridine chemisorbed on Lewis acid

sites (L) could be clearly observed, indicating that only Lewis acidity is present [35,44]. Notably, the relative intensity of adsorption band at  $1450\text{ cm}^{-1}$  is stronger on  $\text{Cu}/\text{ZnAlO}_x$  than that of  $\text{Cu}/\text{MgAlO}_x$ , suggesting that higher acidity is observed for the  $\text{Cu}/\text{ZnAlO}_x$  catalyst.

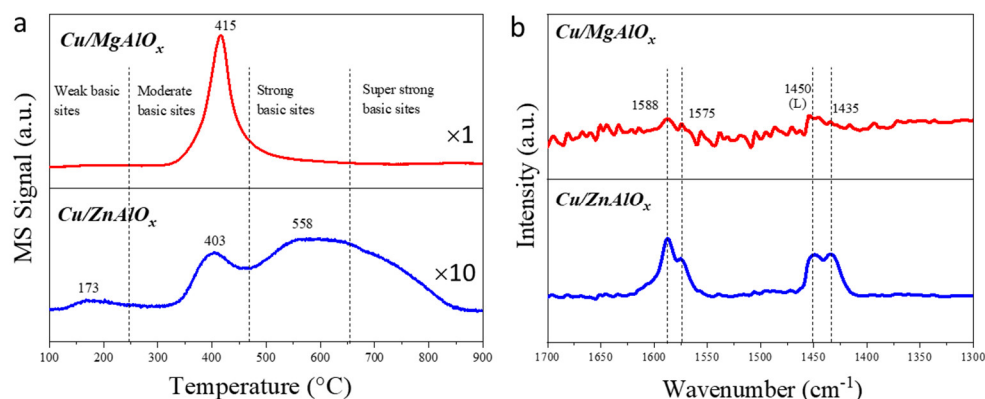


**Figure 6.** (a) CO<sub>2</sub> TPD profile and (b) pyridine adsorbed FT-IR spectra of the supported Cu catalysts.

### 2.5. In Situ Drift Spectra of Ethanol Adsorption and Transformation

In situ DRIFT spectra of ethanol adsorption and transformation for the  $\text{Cu}/\text{MgAlO}_x$  and  $\text{Cu}/\text{ZnAlO}_x$  catalysts were performed and are displayed in Figure 7. With the temperature increasing from 298 K to 573 K, ethanol gradually converted into different intermediates and products for the above catalysts, directly reflecting the reaction of the Guerbet coupling process. For  $\text{Cu}/\text{MgAlO}_x$  (Figure 7a), the bands at  $1252\text{ cm}^{-1}$  are observed at 298 K, which is assigned to the  $\delta(\text{C-OH})$  of adsorbed 3-hydroxybutanal [45], whereas for  $\text{Cu}/\text{ZnAlO}_x$  (Figure 7b), the vibration at  $1393\text{ cm}^{-1}$  could be discerned, indicating the presence of ethyl-acetate species [46]. In addition, the bands at  $1076$  and  $1102\text{ cm}^{-1}$  were presented in both  $\text{Cu}/\text{MgAlO}_x$  and  $\text{Cu}/\text{ZnAlO}_x$  catalysts, corresponding to C-O stretching vibrations in adsorbed ethoxide [27,41]. The  $\text{Cu}/\text{ZnAlO}_x$  catalyst has higher intensity of adsorbed ethoxide at the elevated temperatures, implying that it is more difficult for ethanol transformation for  $\text{Cu}/\text{ZnAlO}_x$  than for  $\text{Cu}/\text{MgAlO}_x$ . The results were in accordance with the catalytic performance (Table 1 and Figure 1). Additionally, as the test temperature increased from 298 K to 523 K, two new bands positioned at  $1645$  and  $1754\text{ cm}^{-1}$  were produced, which is due to the stretching vibrations of C=C group and C=O group in adsorbed crotonaldehyde [27,47]. Furthermore, with the reaction temperature further increased to 573 K, the peaks at  $1645$  and  $1754\text{ cm}^{-1}$  become more prominent for  $\text{Cu}/\text{MgAlO}_x$ , implying the intermediate of crotonaldehyde is easier to produce on  $\text{Cu}/\text{MgAlO}_x$  on  $\text{Cu}/\text{ZnAlO}_x$ , and probably leads to higher yields of a major product such as butanol (Table 1).

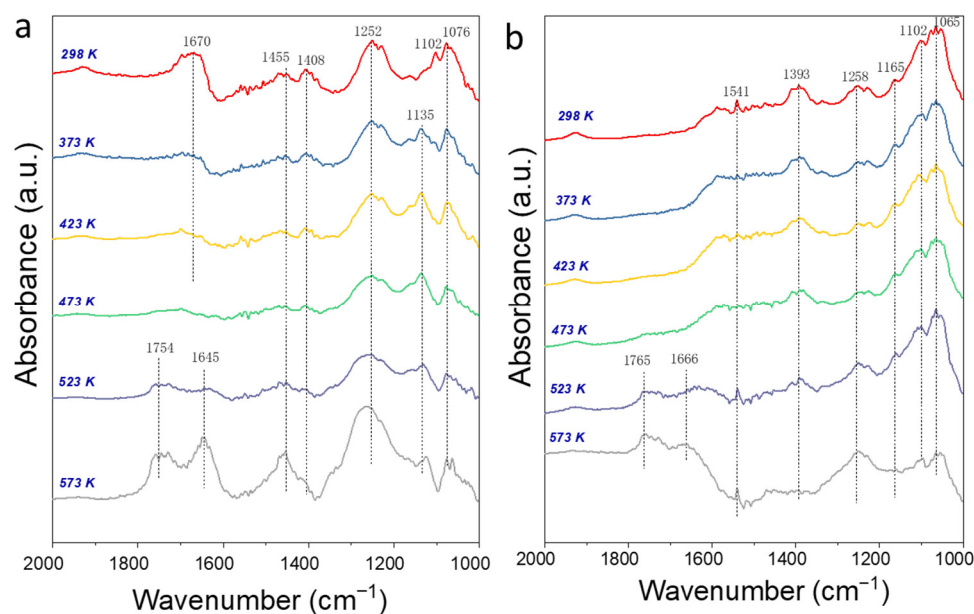


**Figure 7.** In situ drift spectra of ethanol adsorption and transformation on (a) Cu/MgAlO<sub>x</sub> and (b) Cu/ZnAlO<sub>x</sub> catalysts.

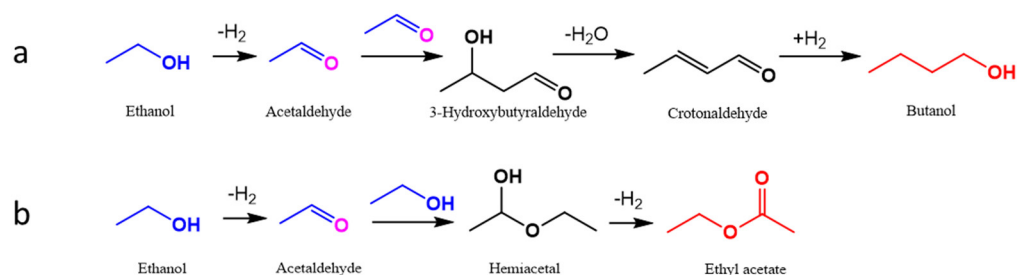
## 2.6. Insight into the Catalytic Performances

According to the catalytic performances on the MgAlO<sub>x</sub> and ZnAlO<sub>x</sub> supported Cu catalysts and the corresponding mixed oxides for ethanol transformation (Table 1 and Figure 1), the active sites were supposed to relate with the Cu species and the supports. Firstly, the structure of Cu species was evaluated by XRD (Figure 3) and TEM (Figure 4) techniques. From the results, Cu species were found highly dispersed on the MgAlO<sub>x</sub> and ZnAlO<sub>x</sub> supports before catalytic performance. After the catalytic test, Cu particles aggregated to larger ones, with the average particle sizes of 6.4 nm for Cu/MgAlO<sub>x</sub> and 4.8 nm for Cu/ZnAlO<sub>x</sub>, respectively (Figure S1). The increased metal particles might account for the decreased activity of both catalysts, especially for Cu/MgAlO<sub>x</sub>. EDX-mapping (Figure S2) and XRD results (Figure S3) indicated the Cu species were still highly dispersed on the catalysts, despite the increased particle sizes.

The valence states of Cu species in the Cu/MgAlO<sub>x</sub> and Cu/ZnAlO<sub>x</sub> catalysts before catalytic tests are mainly Cu<sup>0</sup> and Cu<sup>+</sup>, as displayed by XPS (Figure 5). For Cu/ZnAlO<sub>x</sub>, except for Cu<sup>+</sup>/Cu<sup>0</sup>, Cu<sup>2+</sup> species also existed on the surface. Figure S4 shows the surface composition of Cu/MgAlO<sub>x</sub> and Cu/ZnAlO<sub>x</sub> catalysts after stability tests. The Cu 2p XPS spectra (Figure S4c) indicated the Cu species are all Cu<sup>0</sup>/Cu<sup>+</sup> on Cu/MgAlO<sub>x</sub> and Cu/ZnAlO<sub>x</sub>, as the satellite peaks attributed to Cu<sup>2+</sup> disappeared after catalytic tests. Recently, many researches have reported the supported copper catalysts for the Guerbet coupling process [23,24,27–29]. Cu species in the form of Cu<sup>0</sup>/Cu<sup>+</sup> were proved to have a promotional effect on the rates of reaction steps that involve H-transfers [27,29]. Currently, our group also found that the addition of Cu to the NiAlO<sub>x</sub> could greatly enhance the activity and selectivity of ethanol coupling to butanol [31]. A small amount of Cu<sup>0</sup>/Cu<sup>+</sup> was sufficient for ethanol transformation and to improve the reaction rates of ethanol dehydrogenation [31]. In this work, Cu species with the valence state of Cu<sup>0</sup>/Cu<sup>+</sup> were also considered to be the active sites for H-transfers, because the majority of Cu species for the Cu/MgAlO<sub>x</sub> and Cu/ZnAlO<sub>x</sub> catalysts before and after stability tests are Cu<sup>0</sup> and Cu<sup>+</sup>.

Except for Cu species, the acid-base property resulting from different mixed oxides also plays an important role on the Guerbet coupling process. Previously, large amounts of works presented the conclusions that metal active sites benefit for H-transfers, and acidic-basic sites are in favor of the aldol condensation [27–30]. In this work, based on the results of CO<sub>2</sub>-TPD and pyridine adsorbed FT-IR spectra, the Cu/MgAlO<sub>x</sub> catalyst exhibits

more basic sites, whereas the Cu/ZnAlO<sub>x</sub> catalyst shows more Lewis acid sites (Figure 6). Generally, basic metal oxides were reported active for catalyzing the aldol condensation reaction [44,45], while metal cations as Lewis acid normally in conjugation with basic sites form acid-base pairs for the adsorption and activation of acetaldehyde [48]. Hence, in the Guerbet coupling process, ethanol is dehydrogenated to acetaldehyde for the metal active site, followed by a base-catalyzed aldol coupling reaction to form 3-hydroxybutyraldehyde, then 3-hydroxybutyraldehyde dehydration to crotonaldehyde, and finally hydrogenation to butanol (Scheme 1a) [28,48]. For Cu/MgAlO<sub>x</sub>, sufficient basic sites made it a good candidate for production of butanol. Nevertheless, in synthesis of ethyl acetate, ethanol is firstly dehydrogenated to form acetaldehyde, then acetaldehyde is condensed with ethanol to form hemiacetal, and finally the hemiacetal dehydrogenated to form ethyl acetate (Scheme 1b) [14,49]. As Lewis acid sites can benefit for the adsorption and activation of acetaldehyde, more ethyl acetate would be generated on the acidic Cu/ZnAlO<sub>x</sub> catalyst [14,32,48]. In situ drifts of ethanol (Figure 7) reveal the dynamic reaction process in the Cu/MgAlO<sub>x</sub> and Cu/ZnAlO<sub>x</sub> catalysts, which is in agreement with the catalytic performance. The above results strongly suggest the synergic effect between Cu and mixed metal oxides plays an exclusive role in determining the products distribution in the Guerbet coupling reaction.



**Scheme 1.** The proposed mechanisms for synthesis of (a) butanol and (b) ethyl acetate for the Cu/MgAlO<sub>x</sub> and Cu/ZnAlO<sub>x</sub> catalysts.

### 3. Materials and Methods

#### 3.1. Chemicals

Copper nitrate trihydrate (Cu(NO<sub>3</sub>)<sub>2</sub>·3H<sub>2</sub>O, >99.5%), magnesium nitrate hexahydrate (Mg(NO<sub>3</sub>)<sub>2</sub>·6H<sub>2</sub>O, 99%), zinc nitrate hydrate ((Zn(NO<sub>3</sub>)<sub>2</sub>·6H<sub>2</sub>O), 99 wt%), and aluminum nitrate hexahydrate (Al(NO<sub>3</sub>)<sub>3</sub>·9H<sub>2</sub>O, 99%) were purchased from Sinopharm Chemical Reagent Co. LTD (Shanghai, China). Ethanol (≥99.8%), butanol (>99.5%), methanol (≥99.5%), sodium hydroxide (NaOH, ≥96.0%), sodium carbonate (Na<sub>2</sub>CO<sub>3</sub>, ≥99.8%), ethyl acetate (≥99.7%), and ortho-xylene (≥99.5%) were purchased from Aladdin Industrial Corporation (Shanghai, China). All chemicals were used as received and without any purification. All glassware was washed with Aqua Regia and rinsed with ethanol and ultrapure water. Ultrapure water (18.2 MΩ) was used throughout this work.

#### 3.2. Preparation of the Supported Cu Catalysts

Hydrotalcite (HT) supports of MgAl-HT and ZnAl-HT were synthesized through coprecipitation method with Mg(Zn)/Al molar ratio of 3. In a typically synthesis, a certain amount of Mg(NO<sub>3</sub>)<sub>2</sub>·6H<sub>2</sub>O or Zn(NO<sub>3</sub>)<sub>2</sub>·6H<sub>2</sub>O (0.21 mol) and Al(NO<sub>3</sub>)<sub>3</sub>·9H<sub>2</sub>O (0.07 mol) were dissolved in 200 mL of deionized water to get solution A. Then, a certain amount of NaOH (0.438 mol) and Na<sub>2</sub>CO<sub>3</sub> (0.113 mol) were dissolved in 200 mL of deionized water to get solution B. Under vigorous stirring at 75 °C, solution A was dropwise added into solution B with a constant flow of 3 mL/min, and then the mixture was aged at 75 °C for 24 h. The obtained suspension was filtered and washed for several times with deionized water, and dried overnight at 80 °C to obtain the MgAl-HT and ZnAl-HT.

Supported copper catalysts were synthesized through hydrothermal deposition precipitation method, with the theoretical loadings of 1 wt.%. At first, 2 g of the HT supports and 100 mL of deionized water were added into a round-bottom flask. By using the 0.16 M of  $\text{Na}_2\text{CO}_3$ , the pH value of the solution was adjusted to about 10. Then, 75 mg of  $\text{Cu}(\text{NO}_3)_2 \cdot 3\text{H}_2\text{O}$  was added into the flask and the solution was heated up to 80 °C. The mixture was stirred at 80 °C for 2 h, and the products were filtered and washed with deionized water. Before the test, the samples were dried at 80 °C overnight and calcined at 300 °C for 2 h. The obtained supported Cu catalysts were denoted as Cu/MgAlO<sub>x</sub> and Cu/ZnAlO<sub>x</sub>.

### 3.3. Catalytic Test

The catalytic conversion of ethanol into other products was carried out in a stainless steel fixed-bed reactor (inner diameter: 10 mm, length: 660 mm) equipped with a thermocouple and a mass flow controller. The reaction was performed at 280 °C with N<sub>2</sub> as the carrier gas. Prior to the test, 1 g of the catalyst was loaded into the middle of the reactor, with quartz sand to transfer mass and heat. Then, the pressure of system was increased and maintained with a back-pressure regulator, with a gas hourly space velocity (GHSV) of 692 h<sup>-1</sup>. After purging with N<sub>2</sub> for 0.5 h, the temperature was programmatically increased to 280 °C, with heating rate of 5 °C/min. Then, ethanol was introduced into the system by using a plunger pump (NP-KX-210) with liquid hourly space velocity (LHSV) of 4.8 h<sup>-1</sup>. The reaction products were analyzed offline with an Agilent 7890B chromatograph equipped with an HP-5 capillary column (30 m × 0.32 mm) and a flame ionization detector (FID). O-xylene was used as an internal standard for the quantification of the liquid products.

For the catalytic conversion of ethanol, the conversion was calculated as moles of ethanol reacted to the moles of ethanol fed to the reactor. The selectivity of each product was calculated as moles of carbon in the target product to the moles of carbon in the ethanol reacted. These calculations can be given by the following equations:

$$\text{Conversion (\%)} = \frac{\text{Moles of ethanol reacted}}{\text{Moles of ethanol fed to the reactor}} \times 100$$

$$\text{Selectivity (\%)} = \frac{\text{Moles of carbon in the target product}}{\text{Moles of carbon in ethanol reacted}} \times 100$$

### 3.4. Characterizations

The actual loadings of Cu for the catalysts were measured with an inductively coupled plasma atomic emission spectroscopy (ICP-AES) on an IRIS Intrepid II XSP instrument (Thermo Electron Corporation, Madison, WI, USA).

N<sub>2</sub>-physical adsorption-desorption tests were measured at 77 K using an AutoSorb-1 instrument. Prior to the measurements, the catalysts were treated at vacuum for 2 h at 120 °C. The pore size distribution and the specific surface area were calculated by the BJH and BET methods.

X-ray powder diffraction (XRD) patterns were conducted on a PW3040/60 X'Pert PRO (PANalytical, Almelo, Netherlands) diffractometer, equipped with a Cu K $\alpha$  radiation source ( $\lambda = 0.15432$  nm) operating at 40 kV and 40 mA.

Scanning transmission electron microscopy (STEM) measurements were conducted on a JEM-2100F microscope at 200 kV equipped with an energy dispersive X-ray (EDX) spectrometer. The samples were prepared by dispersing the catalyst powder in ethanol via ultra-sonication onto a micro molybdenum TEM grid.

The X-ray photoelectron spectra (XPS) were conducted on a Thermo ESCALAB 250 X-ray spectrometer (Thermo Fisher Scientific, Madison, WI, USA) equipped with a monochromated Al K $\alpha$  anode. The binding energies were calibrated for surface charging by referencing them to the energy of the C 1s peak at 284.8 eV.

The temperature-programmed desorption of carbon dioxide (CO<sub>2</sub>-TPD) experiments were performed on an AutochemII 2920 instrument (Norcross, GA, USA) with a thermal conductivity detector and mass spectrometry. Before the test, 100 mg of the catalysts were added into a U-type quartz tube reactor. Then the samples were heated in a flow of helium at 300 °C for 30 min. After the temperature decreased to 100 °C, pulses of CO<sub>2</sub> were introduced up to saturation of the sample. Then, the CO<sub>2</sub>-TPD signal were recorded from 100 °C to 900 °C at a rate of 10 °C /min with a cold trap. The signal of the desorbed CO<sub>2</sub> was also recorded by the MS simultaneously.

Pyridine adsorbed Fourier-transformed infrared absorption spectra were conducted on a Bruker INVENIO spectrometer (Karlsruhe, Germany), equipped with a MCT detector in the range of 1000~4000 cm<sup>-1</sup>. Each spectrum was collected with a resolution of 4 cm<sup>-1</sup> and 32 scans. Self-supported catalyst wafers (~0.15 g) were pressed and placed into a in situ IR cell with a CaF<sub>2</sub> window. Before the test, the cell was vacuumed to 10<sup>-3</sup> torr, and the catalyst was treated at 200 °C for 30 min with a heating ramp of 5 °C/min. After cooling to room temperature, the background spectrum was collected under vacuum condition at 25 °C, and then the sample was exposed to pyridine vapor until adsorption saturation. Finally, the adsorbed pyridine was desorbed at 100 °C until the spectra showed no change.

In situ diffuse reflectance infrared Fourier-transformed spectroscopy (DRIFTS) was also performed on a Bruker INVENIO spectrometer (Bruker, Karlsruhe, Germany). Prior to the test, the catalyst was packed into a in situ cell with a ZnSe window and treated at 300 °C for 0.5 h. After cooling to 25 °C, the background spectrum was recorded under atmospheric pressure in helium. Then, ethanol was introduced into the cell with the assistance of helium. Finally, the reaction temperature was programmatically increased to the fixed temperatures, with a heating rate of 10 °C/min. After achieving the steady state, the spectra were collected at 100, 150, 200, 250, and 300 °C, respectively.

#### 4. Conclusions

In summary, MgAlO<sub>x</sub> and ZnAlO<sub>x</sub> mixed-oxides supported Cu catalysts were used for ethanol conversion via Guerbet coupling reaction. The two catalysts show obvious different performances under identical reaction conditions. For Cu/MgAlO<sub>x</sub>, conversion of ethanol and selectivity of butanol were 43.1% and 33.2%, respectively, whereas for Cu/ZnAlO<sub>x</sub>, the major product is ethyl acetate, with conversion and selectivity of 33.9% and 42.2%, respectively. The sole mixed-oxides were also conducted to make a comparison, from which low activity was observed in both catalysts, indicating a great influence of Cu species for ethanol transformation. The acid-base sites resulting from different mixed oxides might determine the distribution of products, from which the catalysts with appropriate basic sites were beneficial to form the condensation products such as crotonaldehyde and butanol, whereas the catalysts with more acid sites were believed to form dehydrogenation products, such as ethyl acetate. In combination the catalytic performances with the characterization results, the synergistic effect between Cu species with the acid-base sites were deduced to be the active sites. This work will provide good reference for designing supported metal catalyst for the Guerbet coupling process with good activity and high product selectivity.

**Supplementary Materials:** The following are available online at <https://www.mdpi.com/article/10.3390/catal12101170/s1>, Figure S1: XPS spectra of supported Cu catalysts after stability test; Figure S2: XRD patterns of supported Cu catalysts after stability test; Figure S3: TEM and HRTEM images of different supported Cu catalysts after stability test; Figure S4: EDX-mapping of Cu/MgAlO<sub>x</sub> catalyst after stability test.

**Author Contributions:** Y.T. and Y.D. conceived of the study; Z.L. and J.L. performed most of the experiments; L.G. contributed with some of the characterizations. All the authors contributed to the writing of the manuscript. All authors have read and agreed to the published version of the manuscript.

**Funding:** This research was supported by the National Natural Science Foundation of China under Grant No. 22102149.

**Acknowledgments:** The authors appreciate the support from the public testing platform of Zhejiang Normal University and Dalian Institute of Chemical Physics, Chinese Academy of Sciences. Thanks for the technical support with ICP, XRD, TEM, HRTEM, and XPS measurements.

**Conflicts of Interest:** The authors declare no conflict of interest.

## References

1. Aitchison, H.; Wingad, R.L.; Wass, D.F., Homogeneous Ethanol to Butanol Catalysis-Guerbet Renewed. *ACS Catal.* **2016**, *6*, 7125–7132.
2. Angelici, C.; Weckhuysen, B.M.; Bruijninx, P.C.A. Chemocatalytic Conversion of Ethanol into Butadiene and Other Bulk Chemicals. *ChemSusChem* **2013**, *6*, 1595–1614.
3. Phillips, S.D.; Jones, S.B.; Meyer, P.A.; Snowden-Swan, L.J. Techno-economic analysis of cellulosic ethanol conversion to fuel and chemicals. *Biofuels Bioprod. Bioref.* **2022**, *16*, 640–652.
4. Hamelinck, C.N.; Hooijdonk, G.; Faaij, A.P.C. Ethanol from lignocellulosic biomass: Techno-economic performance in short-, middle- and long-term. *Biomass Bioenergy* **2005**, *28*, 384–410.
5. Rass-Hansen, J.; Falsig, H.; Jørgensen, B.; Christensen, C.H. Perspective Bioethanol: Fuel or feedstock? *Chem. Technol. Biotechnol.* **2007**, *82*, 329–333.
6. Szulczyk, K.R. Which is a better transportation fuel-Butanol or ethanol? *Int. J. Hydrog. Energy* **2010**, *3*, 501–512.
7. Dziugan, P.; Jastrzabek, K.G.; Binczarski, M.; Karski, S.; Witonska, I.A.; Kolesinska, B.; Kaminski, Z.J. Continuous catalytic coupling of raw bioethanol into butanol and higher homologues. *Fuel* **2015**, *158*, 81–90.
8. Carvalho, D.L.; Avillez, R.R.; Rodrigues, M.T.; Borges, L.E.P.; Appel, L.G. Mg and Al mixed oxides and the synthesis of n-butanol from ethanol. *Appl. Catal. A Gen.* **2012**, *415–416*, 96–100.
9. Chistyakov, A.V.; Nikolaev, S.A.; Zharova, P.A.; Tsodikov, M.V.; Manenti, F. Linear  $\alpha$ -alcohols production from supercritical ethanol over Cu/Al<sub>2</sub>O<sub>3</sub> catalyst. *Energy* **2019**, *166*, 569–576.
10. Pacheco, H.P.; Souza, E.F.; Landi, S.M.; David, M.V.; Prillaman, J.T.; Davis, R.J.; Toniolo, F.S. Ru Promoted MgO and Al-Modified MgO for Ethanol Upgrading. *Top. Catal.* **2019**, *62*, 894–907.
11. Osman, M.B.; Krafft, J.M.; Thomas, C.; Yoshioka, T.; Kubo, J.; Costentin, G. Importance of the Nature of the Active Acid/Base Pairs of Hydroxyapatite Involved in the Catalytic Transformation of Ethanol to n-Butanol Revealed by Operando DRIFTS. *ChemCatChem* **2019**, *11*, 1–15.
12. León, M.; Díaz, E.; Ordóñez, S. Ethanol catalytic condensation over Mg–Al mixed oxides derived from hydrotalcites. *Catal. Today* **2011**, *164*, 436–442.
13. Neumann, C.N.; Payne, M.T.; Rozeveld, S.J.; Wu, Z.; Zhang, G.; Comito, R.J.; Miller, J.T.; Dincă, M. Structural Evolution of MOF-Derived RuCo, A General Catalyst for the Guerbet Reaction. *ACS Appl. Mater. Interfaces* **2021**, *13*, 52113–52124.
14. Mück, J.; Kocík, J.; Hájek, M.; Tišler, Z.; Frolich, K.; Kašpárek, A. Transition metals promoting Mg–Al mixed oxides for conversion of ethanol to butanol and other valuable products: Reaction pathways. *Appl. Catal. A Gen.* **2021**, *626*, 118380.
15. López-Olmos, C.; Morales, M.V.; Guerrero-Ruiz, A.; Ramirez-Barria, C.; Asedegbega-Nieto, E.; Rodríguez-Ramos, I. Continuous gas phase condensation of bioethanol to 1-butanol over bifunctional Pd/Mg and Pd/Mg-carbon catalysts. *ChemSusChem* **2018**, *11*, 3502–3511.
16. Nikolaev, S.A.; Tsodikov, M.V.; Chistyakov, A.V.; Zharova, P.A.; Ezzgelenko, D.I. The activity of mono- and bimetallic gold catalysts in the conversion of sub- and supercritical ethanol to butanol. *J. Catal.* **2019**, *369*, 501–507.
17. Wu, X.; Fang, G.; Liang, Z.; Leng, W.; Xu, K.; Jiang, D.; Ni, J.; Li, X. Catalytic upgrading of ethanol to n-butanol over M-CeO<sub>2</sub>/AC (M=Cu, Fe, Co, Ni and Pd) catalysts. *Catal. Commun.* **2017**, *100*, 15–18.
18. Fu, S.; Shao, Z.; Wang, Y.; Liu, Q. Manganese-Catalyzed Upgrading of Ethanol into 1-Butanol. *J. Am. Chem. Soc.* **2017**, *139*, 11941–11948.
19. Perrone, O.M.; Lobefaro, F.; Aresta, M.; Nocito, F.; Boscolo, M.; Dibenedetto, A. Butanol synthesis from ethanol over CuMgAl mixed oxides modified with palladium (II) and indium (III). *Fuel Process. Technol.* **2018**, *177*, 353–357.
20. Hanspal, S.; Young, Z.D.; Prillaman, J.T.; Davis, R.J. Influence of surface acid and base sites on the Guerbet coupling of ethanol to butanol over metal phosphate catalysts. *J. Catal.* **2017**, *352*, 182–190.
21. Tsuchida, T.; Sakuma, S.; Takeguchi, T.; Ueda, W. Direct Synthesis of n-Butanol from Ethanol over Nonstoichiometric Hydroxyapatite. *Ind. Eng. Chem. Res.* **2006**, *45*, 8634–8642.
22. Ogo, S.; Onda, A.; Yanagisawa, K. Selective synthesis of 1-butanol from ethanol over strontium phosphate hydroxyapatite catalysts. *Appl. Catal. A Gen.* **2011**, *402*, 188–195.
23. IMarcu, C.; Tichit, D.; Fajula, F.; Tanchoux, N. Catalytic valorization of bioethanol over Cu–Mg–Al mixed oxide catalysts. *Catal. Today* **2019**, *147*, 231–238.
24. Jiang, D.; Wu, X.; Mao, J.; Ni, J.; Li, X. Continuous catalytic upgrading of ethanol to n-butanol over Cu–CeO<sub>2</sub>/AC catalysts. *Chem. Commun.* **2016**, *52*, 13749.

25. Wang, Z.; Pang, J.; Song, L.; Li, X.; Yuan, Q.; Li, X.; Liu, S.; Zheng, M. Conversion of Ethanol to n-Butanol over NiCeO<sub>2</sub> Based Catalysts: Effects of Metal Dispersion and NiCe Interactions. *Ind. Eng. Chem. Res.* **2020**, *59*, 22057–22067.
26. Yang, C.; Meng, Z.Y. Bimolecular Condensation of Ethanol to 1-Butanol Catalyzed by Alkali Cation Zeolites. *J. Catal.* **1993**, *142*, 37–44.
27. Wang, Z.; Yin, M.; Pang, J.; Li, X.; Xing, Y.; Su, Y.; Liu, S.; Liu, X.; Wu, P.; Zheng, M.; et al. Active and stable Cu doped NiMgAlO catalyzers for upgrading ethanol to n-butanol. *J. Energy Chem.* **2022**, *72*, 306–317.
28. Cuello-Penaloza, P.A.; Dastidar, R.G.; Wang, S.C.; Du, Y.; Lanci, M.P.; Wooller, B.; Kliewer, C.E.; Hermans, I.; Dumesic, J.A.; Huber, G.W. Ethanol to distillate-range molecules using Cu/Mg<sub>x</sub>AlO<sub>y</sub> catalysts with low Cu loadings. *Appl. Catal. B Environ.* **2022**, *304*, 120984.
29. Zhou, J.; He, Y.; Xue, B.; Cheng, Y.; Zhou, D.; Wang, D.; He, Y.; Guan, W.; Fang, K.; Zhang, L.; et al. Benefits of active site proximity in Cu@UiO-66 catalysts for efficient upgrading of ethanol to nbutanol. *Sustain. Energy Fuels* **2021**, *5*, 4628.
30. Jiang, D.; Fang, G.; Tong, Y.; Wu, X.; Wang, Y.; Hong, D.; Leng, W.; Liang, Z.; Tu, P.; Liu, L.; et al. Multifunctional Pd@UiO-66 Catalysts for Continuous Catalytic Upgrading of Ethanol to n-Butanol. *ACS Catal.* **2018**, *8*, 11973–11978.
31. Li, J.; Lin, L.; Tan, Y.; Wang, S.; Yang, W.; Chen, X.; Luo, W.; Ding, Y. High performing and stable Cu/NiAlO<sub>x</sub> catalysts for the continuous catalytic conversion of ethanol into butanol. *ChemCatChem* **2022**, *14*, e202200539.
32. Gao, D.; Feng, Y.; Yin, H.; Wang, A.; Jiang, T. Coupling reaction between ethanol dehydrogenation and maleic anhydride hydrogenation catalyzed by Cu/Al<sub>2</sub>O<sub>3</sub>, Cu/ZrO<sub>2</sub>, and Cu/ZnO catalysts. *Chem. Eng. J.* **2013**, *233*, 349–359.
33. Cheng, F.; Guo, H.; Cui, J.; Hou, B.; Li, D. Guerbet reaction of methanol and ethanol catalyzed by CuMgAlO<sub>x</sub> mixed oxides: Effect of M<sup>2+</sup>/Al<sup>3+</sup> ratio. *J. Fuel Chem. Technol.* **2018**, *46*, 1472–1481.
34. Petrolini, D.D.; Eagan, N.; Ball, M.R.; Burt, S.P.; Hermans, I.; Huber, G.W.; Dumesic, J.A.; Martins, L. Ethanol condensation at elevated pressure over copper on AlMgO and AlCaO porous mixed-oxide supports. *Catal. Sci. Technol.* **2019**, *9*, 2032.
35. Zhu, Q.; Yin, L.; Ji, K.; Li, C.; Wang, B.; Tan, T. Effect of Catalyst Structure and Acid–Base Property on the Multiproduct Upgrade of Ethanol and Acetaldehyde to C<sub>4</sub> (Butadiene and Butanol) over the Y–SiO<sub>2</sub> Catalysts. *ACS Sustain. Chem. Eng.* **2020**, *8*, 1555–1565.
36. Sing, K.S.W.; Williams, R.T. Physisorption Hysteresis Loops and the Characterization of Nanoporous Materials. *Adsorpt. Sci. Technol.* **2004**, *22*, 773–782.
37. Martunus; Othman, M.R.; Fernando, W.J.N. Elevated temperature carbon dioxide capture via reinforced metal hydrotalcite. *Micropor. Mesopor. Mater.* **2011**, *138*, 110–117.
38. Sutthiumporn, K.; Kawi, S. Promotional effect of alkaline earth over Ni-La<sub>2</sub>O<sub>3</sub> catalyst for CO<sub>2</sub> reforming of CH<sub>4</sub>: Role of surface oxygen species on H<sub>2</sub> production and carbon suppression. *Int. J. Hydrog. Energ.* **2011**, *36*, 14435–14446.
39. Pang, J.; Zheng, M.; Wang, C.; Yang, X.; Liu, H.; Liu, X.; Sun, J.; Wang, Y.; Zhang, T. Hierarchical Echinus-like Cu-MFI Catalysts for Ethanol Dehydrogenation. *ACS Catal.* **2020**, *10*, 13624–13629.
40. Wang, L.; Zhu, W.; Zheng, D.; Yu, X.; Cui, J.; Jia, M.; Zhang, W.; Wang, Z. Direct transformation of ethanol to ethyl acetate on Cu/ZrO<sub>2</sub> catalyst. *React. Kinet. Mech. Cat.* **2010**, *101*, 365–375.
41. Zhang, J.; Shi, K.; Zhu, Y.; An, Z.; Wang, W.; Ma, X.; Shu, X.; Song, H.; Xiang, X.; He, J. Interfacial Sites in Ag Supported Layered Double Oxide for Dehydrogenation Coupling of Ethanol to n-Butanol. *ChemistryOpen* **2021**, *10*, 1095–1103.
42. Li, H.; Tan, Y.; Chen, X.; Yang, W.; Huang, C.; Li, J.; Ding, Y. Efficient Synthesis of Methyl Methacrylate by One Step Oxidative Esterification over Zn-Al-Mixed Oxides Supported Gold Nanocatalysts. *Catalysts* **2021**, *11*, 162.
43. Gao, J.; Fan, G.; Yang, L.; Cao, X.; Zhang, P.; Li, F. Oxidative Esterification of Methacrolein to Methyl Methacrylate over Gold Nanoparticles on Hydroxyapatite. *ChemCatChem* **2017**, *9*, 1230–1241.
44. Liang, Z.; Jiang, D.; Fang, G.; Leng, W.; Tu, P.; Tong, Y.; Liu, L.; Ni, Jun.; Li, X. Catalytic Enhancement of Aldol Condensation by Oxygen Vacancy on CeO<sub>2</sub> Catalysts. *ChemistrySelect* **2019**, *4*, 4364–4370.
45. Zhang, J.; Shi, K.; An, Z.; Zhu, Y.; Shu, X.; Song, H.; Xiang, X.; He, J. Acid–Base Promoted Dehydrogenation Coupling of Ethanol on Supported Ag Particles. *Ind. Eng. Chem. Res.* **2020**, *59*, 3342–3350.
46. Pinzón, M.; Cortés-Reyes, M.; Herrera, C.; Larrubia, M.Á.; Alemany, L.J. Ca-based bifunctional acid-basic model-catalysts for n-butanol production from ethanol condensation. *Biofuels Bioprod. Bior.* **2021**, *15*, 218–230.
47. Yuan, B.; Zhang, J.; An, Z.; Zhu, Y.; Shu, X.; Song, H.; Xiang, X.; Wang, W.; Jing, Y.; Zheng, L.; et al. Atomic Ru catalysis for ethanol coupling to C<sub>4</sub> alcohols. *Appl. Catal. B* **2022**, *309*, 121271.
48. Tong, Y.; Zhou, J.; He, Y.; Tu, P.; Xue, B.; Cheng, Y.; Cen, J.; Zheng, Y.; Ni, J.; Li, X. Structure-activity relationship of Cu species in the ethanol upgrading to n-butanol. *ChemistrySelect* **2020**, *5*, 7714–7719.
49. Riittonen, T.; Toukoniitty, E.; Madnani, D.K.; Leino, A.R.; Kordas, K.; Szabo, M.; Sapi, A.; Arve, K.; Wärnå, J.; Mikkola, J.P. One-pot liquid-phase catalytic conversion of ethanol to 1-butanol over aluminium oxide—The effect of the active metal on the selectivity. *Catalysts* **2012**, *2*, 68–84.